RSC Advances

ROYAL SOCIETY OF CHEMISTRY

PAPER

View Article Online
View Journal | View Issue

Cite this: *RSC Adv.*, 2021, **11**, 781

Facile synthesis of superparamagnetic Fe_3O_4@noble metal core–shell nanoparticles by thermal decomposition and hydrothermal methods: comparative study and catalytic applications†

Eman A. Bakr,* Marwa N. El-Nahass,* Wafaa M. Hamada and Tarek A. Fayed

Herein, we report on developing a facile synthetic route for reusable nanocatalysts based on a combination of the supermagnetic properties of magnetite with the unique optical and catalytic properties of noble metal hybrid nanomaterials. We compare two different synthetic methods, to find out which is best from synthetic and application points of view, for the synthesis of Fe_3O_4 and Fe_3O_4@M (M = Ag or Au) core–shell hybrid nanostructures. The two different single-step synthetic methods are: thermal decomposition and hydrothermal. The structural, morphological and magnetic properties of the obtained Fe_3O_4 and Fe_3O_4@M nanoparticles were characterized by various techniques. XRD of the Fe_3O_4 nanoparticles exhibited sharp and strong diffraction peaks, confirming the highly crystalline structure of the Fe_3O_4 particles synthesized by the hydrothermal method, while broad and weak peaks were observed on using the thermal decomposition method. Both Fe_3O_4@Ag and Fe_3O_4@Au core–shells obtained by the hydrothermal method showed the reflection planes of Fe_3O_4 and additional planes of Ag or Au. But on the formation of Fe_3O_4@Ag/Au by the thermal decomposition method the peak for Fe_3O_4 disappeared and only the diffraction peaks of Ag or Au appeared. According to TEM analysis there was a broad particle-size distribution, random near-spherical shapes and slight particle agglomeration for Fe_3O_4 synthesized by the thermal decomposition method. However, there was a moderate size distribution, spherical shapes and well-dispersed particles without large aggregations for the hydrothermal method. TEM images of the synthesized nanoparticles by the two methods used showed a pronounced difference in both size and morphological shape. The catalytic performance of the synthesized nanoparticles was examined for the reduction of Congo red dye in the presence of $NaBH_4$. The Fe_3O_4 nanocatalyst maintained its catalytic activity for only one cycle. In the cases of Fe_3O_4@Au and Fe_3O_4@Ag, the catalytic activity was conserved for four and ten successive cycles, respectively. Based on the obtained results, it was concluded that the hydrothermal synthesis of Fe_3O_4, Fe_3O_4@Ag and Fe_3O_4@Au nanostructures is highly recommended due to their selectivity and merits.

Received 25th September 2020
Accepted 24th November 2020

DOI: 10.1039/d0ra08230a

rsc.li/rsc-advances

1. Introduction

Core–shell hybrid nanoparticles formed from the combination of two or more types of nanoparticles are highly regarded by the scientific community. They have the potential to merge the unique physicochemical properties of two or more nanomaterials into one entity, leading to enormous advances by these structures towards various applications in the areas of catalysis, electronics, photonics, and biotechnology and environmental applications.[1–7] Superparamagnetic Fe_3O_4 has found applications in medicine for drug transport as a local magnetic therapy, to diagnose and treat cancer using magnetic hyperthermia (ablation), for magnetic marking of cells (immunological separation) or for contrast strengthening in cell magnetic resonance imaging.[8,9] Among these applications catalysis technologies are chosen to contribute to alleviation of the water pollution problem. It is a global issue and the world community is facing the worst effects of polluted water. One of the major sources of water pollution is the discharge of organic dyes as industrial waste. There is an urgent need to find an ideal remover that not only reduces these organic dyes but also achieves their selective separation and recovery to achieve a green chemistry concept. So, it is of utmost importance to develop new materials with tailored properties that can meet strong

Department of Chemistry, Faculty of Science, Tanta University, 31527, Tanta, Egypt. E-mail: marwa.elnahas@science.tanta.edu.eg; eman.bakr@science.tanta.edu.eg; Fax: +20-403350804; Tel: +20-403344352

† Electronic supplementary information (ESI) available. See DOI: 10.1039/d0ra08230a

connections between eco-efficiency and performance, processing and manufacturing, recyclability, and costs. Actually, through nanocomposites with core–shell nanostructures, the catalytic properties can be enhanced to a great extent, which may not be achievable by the use of monometallic catalysts. Magnetic iron oxide nanoparticles (MIONPs) are ideal materials for industrial and biomedical applications because of their very low toxicity and biodegradability.[10–15] Superparamagnetic iron oxide nanoparticles, such as magnetite nanoparticles (Fe_3O_4), are extremely attractive as a component of core–shell hybrid nanoparticles where the saturation magnetization value for the bulk material is 92 emu g^{-1}, so they connect with external fields, providing them with the capability to be easily recovered and subsequently reused or else pulled by a magnetic bar.[16,17] However, Fe_3O_4 nanoparticles have large specific surface areas; they are prone to oxidation and aggregation leading to low magnetism and poor dispersion. Recently, attempts have been made to apply certain facial modifications to Fe_3O_4 through the development of a wide range of hybrid nanoparticles.[18] Distinct consideration is being paid now to the effect of noble metals, such as Ag and Au NPs, on the properties of Fe_3O_4, due to their specific characteristics like: (i) intense absorption in the optical region associated with localized surface plasmon resonance (LSPR),[19] and (ii) their stability at high temperatures under conditions where base metals are rapidly oxidized.[20] This was confirmed by an improvement in the stability of and an enhancement in the catalytic and antibacterial activities of the Fe_3O_4@noble metal hybrid nanoparticles, suggesting their importance for potential applications in water treatment and biomedicine.[21–24] A wide variety of types of chemical processing can be used to synthesize hybrid nanoparticles, such as co-precipitation, thermal decomposition, electrodeposition, sol–gel, sonochemical and hydrothermal methods. Each technique used to produce hybrid nanoparticles has different characteristics and displays some advantages and disadvantages. The selection of a specific technique will be based on several factors, such as the kind of desired structure, the necessity for size control, time available to produce the particles, and the required interaction between both components. Thermal decomposition is a common method used in industry to synthesize narrow magnetic iron oxide nanoparticles (MIONPs). In this method, the iron precursor and reducing agent are injected into a solvent containing surfactant solution at a high temperature, which in turn decomposes the iron precursor in the presence of the surfactant that will coat and stabilize the formation of MIONPs. The thermal decomposition method is characterized by some advantages, in comparison with other methods: the process is non-toxic, inexpensive and achieves high crystallinity with a uniform size distribution, allowing a good amount of nanocrystals to be produced in a single reaction without a further size-sorting process.[25] Hydrothermal synthesis of MIONPs in aqueous media is carried out in autoclaves/reactors at high temperature and pressure (above 200 °C and 13 790 kPa).[26–31] Rapid nucleation and faster growth occur at high temperature and lead to the formation of MIONPs. The crystals formed by hydrothermal treatment are generally narrow with high purity and density. They do not aggregate due to the presence of stabilizing agents.

The main goal of the present study is to optimize a synthetic method for Fe_3O_4@M (M = Ag or Au) core–shell NPs. Herein, we applied two different single-step synthetic methods; (i) thermal decomposition and (ii) hydrothermal, to compare them to find which is better in terms of both synthetic and catalytic approaches. Different complementary analytical tools were used to characterize the synthesized nano-core–shells such as FTIR, XRD, TEM, EDX, UV-Vis, and magnetization. Congo red was selected as a target pollutant, due to its solubility in water and extensive use in the textile, paper, rubber and plastic industries. Congo red is a carcinogenic benzidine-based anionic diazo dye used for the coloration of paper products. The catalytic activities of Fe_3O_4@M core–shell NPs were utilized for the degradation of Congo red dye in aqueous solution using $NaBH_4$ as a reducing agent. The effects of $NaBH_4$, initial dye concentration and catalyst amount on the degradation process were also studied in detail.

2. Experimental

2.1 Materials and reagents

All chemicals were commercial grade and used without additional purification. They include ferric nitrate nonahydrate $Fe(NO_3)_3 \cdot 9H_2O$, silver nitrate $AgNO_3$, tetrachloroauric acid $HAuCl_4 \cdot 3H_2O$, tri-disodium citrate dihydrate $C_6H_5O_7Na_3 \cdot 2H_2O$, urea ($CON_2H_4$), polyacrylamide (PAM), sodium borohydride $NaBH_4$ (99.0%) and Congo red. Deionized water was used for all synthesis and measurement procedures.

2.2 Methods for synthesis of Fe_3O_4, Fe_3O_4@Ag, and Fe_3O_4@Au NPs

2.2.1 Thermal decomposition method. The thermal decomposition method is one of the best developed methods to tune the size and shape of modified iron oxide nanoparticles, MIONPs. Coordination compounds are used as precursors to increase the quality of MIONPs. In this method, an iron coordination compound containing a surfactant solution was injected into a solvent at high temperature, which in turn decomposed, giving an iron precursor in the presence of a surfactant. This coats and stabilizes the formed MIONPs.

2.2.1.1 Synthesis of magnetite nanoparticles (Fe_3O_4). Magnetite nanoparticles were synthesized using an iron–urea complex, iron(III) hexaureatrinitrate $[Fe(CON_2H_4)_6](NO_3)_3$, in the presence of sodium citrate as a stabilizing agent. This route was relatively environmentally-friendly because ferric nitrate and urea were the precursors for the iron complex. In a typical synthesis; 1 mmol $Fe(NO_3)_3 \cdot 9H_2O$, 6.2 mmol urea (CON_2H_4) and 3 mmol sodium citrate ($C_6H_5O_7Na_3 \cdot 2H_2O$) in 1 : 6.2 : 3 molar ratio were dissolved in about 15 mL of distilled water. The obtained light green colored precipitate was vigorously stirred for 1 h. Then 0.15 g of polyacrylamide (PAM) as a capping agent was added under continuous stirring until complete dissolution. The mixture was then taken in a round-bottom flask and refluxed with stirring in the air at 200 °C for about 12 h. After cooling

down to room temperature, the precipitate was collected by magnetic separation, washed several times with ethanol, then with distilled water, and kept in an oven at 40 °C overnight for drying. The prepared sample was calcined at 600 °C in a muffle oven (heating rate = 2 °C min^{-1}) under air atmosphere.

2.2.1.2 Synthesis of core–shell hybrid nanoparticles of Fe_3O_4@M (M = Ag or Au). The preparation of Fe_3O_4@M core–shell nanoparticles was carried out following the same procedures as in Section 2.2.1.1, with only one additional step, where 0.5 mmol $AgNO_3$ was used for the synthesis Fe_3O_4@Ag, and 0.5 mmol $HAuCl_4 \cdot 3H_2O$ for the synthesis Fe_3O_4@Au, where each of these additives was dissolved in 5 mL of distilled water, then dropped slowly into the former solution until it dissolved completely. The molar ratio of the noble metal precursor to that of iron was 1 : 2. The remaining steps were followed exactly until the required product was obtained.

2.2.2 Hydrothermal method. This technique is relatively simple, inexpensive and rapid. It provides highly crystalline Fe_3O_4 nanoparticles with good magnetic properties and high monodispersity,[32,33] because it exploits the solubility of inorganic substances at certain temperatures and high pressures. To achieve a real comparison between this method and the thermal decomposition method, the same reactants were used in the same order, so that the only difference in the resulting product is due to the effect of the method used.

2.2.2.1 Synthesis of magnetite nanoparticles (Fe_3O_4). $Fe(NO_3)_3 \cdot 9H_2O$ (1 mmol), urea (CON_2H_4) (6.2 mmol), and sodium citrate ($C_6H_5O_7Na_3 \cdot 2H_2O$) (3 mmol) were dissolved in about 15 mL of distilled water followed by intensive stirring for 1 h until the reactants were completely converted to a light green precipitate. Then, 0.15 g of polyacrylamide (PAM) was slowly added under vigorous stirring until complete dissolution of all the materials. The solution was subsequently transferred to a 50 mL Teflon-lined autoclave. The autoclave was then sealed and subsequently put into an oven at 200 °C for 12 h. After the autoclave had cooled down to room temperature, the black precipitate was collected by an external magnet, washed alternately with absolute ethanol and distilled water several times, and dried in the oven at 50 °C overnight.

2.2.2.2 Synthesis of core–shell hybrid nanoparticles of Fe_3O_4@M (M = Ag or Au). Fe_3O_4@M core–shell nanoparticles synthesized by the hydrothermal method were achieved by following the same procedures as in Section 2.2.2.1. Then 5 mL of 0.5 mmol aqueous $AgNO_3$ 0.5 mmol $HAuCl_4 \cdot 3H_2O$, for the synthesis of Fe_3O_4@Ag or Fe_3O_4@Au, respectively, were dropped slowly into the formed solution until it had totally dissolved. The same molar ratio of noble metal precursor to iron precursor was taken into account, which was 1 : 2. The remaining steps were followed exactly as previously.

The chemical steps for the synthesis of Fe_3O_4@Ag and Fe_3O_4@Au core–shell nanoparticles by the two investigated methods are shown in Scheme 1.

2.3 Catalytic performance of the synthesized NPs

The catalytic behavior of all synthesized nanostructures has been demonstrated toward the reduction of Congo red dye, CR. CR was not reduced readily in aqueous media by addition of $NaBH_4$ as a reducing agent and the reaction was not kinetically feasible. The reaction mixture consisted of 0.5 mL of dye solution of 1×10^{-3} mol L^{-1}, 5 mL of aqueous solution of 0.05 mol L^{-1} $NaBH_4$ and the solution mixture was brought up to 10 mL using distilled water and then finally 20 mg of nanocatalyst was added. The time-dependent UV/Vis absorption spectra were recorded at 496 nm immediately after the addition of the nanocatalyst into the reaction mixture to follow the reduction process. The decrease in the absorbance of unreduced CR was recorded, until the steady-state was reached.

To follow the progress of CR dye degradation under these conditions, the efficiency percentage was calculated as a function of time. The degradation efficiency was calculated as;[34]

Scheme 1 Schematic representation of the procedures for the synthesis of Fe_3O_4@Ag and Fe_3O_4@Au core–shell NPs by the two methods.

$$\text{Efficiency}\% = \frac{A_0 - A_t}{A_0} \times 100$$

where, A_0 and A_t are the absorbance of the free CR dye and at time t, respectively.

2.4 Instrumentation

An FT-IR-4100 (JASCO, Japan) spectrophotometer was used to record the FT-IR spectra within the range 4000–400 cm^{-1} with a resolution of 2 cm^{-1} using KBr pellets. The crystalline structure of all synthesized nanostructures was analyzed by X-ray powder diffraction (XRD) with a GNR APD 2000 PRO diffractometer in the angular range $2\theta = 5°$–$90°$ at 293 K using nickel-filtered Cu Kα ($\lambda = 1.5405$ Å) radiation operating at 40 kV and 30 mA. The morphology was examined by transmission electronic microscopy (TEM) measurements using a JEOL (Jem-2100) electron microscope (HT 200 eV; resolution 0.1432 nm; option 1.5 million). An energy-dispersive X-ray spectrometer (EDX) IT100LA operating at an accelerating voltage of 20.00 keV was attached to a transmission electron microscope (TEM). Magnetic properties were measured by a vibrating sample magnetometer (VSM, Lake Shore, 7410 model) at room temperature. The thermal analysis, TGA, was carried out in the range 30–800 °C using a Shimadzu TG-50 thermogravimetric analyzer under a nitrogen atmosphere with a heating rate of 20 °C min^{-1}. The UV-Vis absorption spectra were recorded using a Shimadzu double beam UV-Vis Scanning Spectrophotometer (UV-3101 PC), using matched quartz cuvettes.

3. Results and discussion

3.1 Mechanism of formation of Fe_3O_4@M core–shell nanostructures

A possible mechanism for the formation of the Fe_3O_4@M core–shell from the iron–urea complex is depicted in Schemes 2 and 3. It was proposed that cyanuric acid is formed along with iron oxide nanoparticles on the thermal decomposition of the iron–urea complex.[35] The cyanuric acid molecules present on the surface of the iron oxide nanoparticles are hydrogen-bonded to sodium citrate molecules and coat them completely. Citrate and PAM play important roles in the formation of well-defined Fe_3O_4@M core–shell NPs. The polymer, PAM, played two roles in the synthetic route. Firstly, PAM with abundant amide groups is considered to be an efficient chelating agent for the preparation of supported Ag NPs through the coordination of N and O atoms with Ag^+ ions.[36] Secondly, it worked as a capping agent and stabilizer.[37] Due to the large amount of amide ligands, PAM could be adsorbed on the surface of the product, consequently stabilizing the primary formed particles. The increased viscosity slows down the reaction rate as well as the rate of movement of the primary nanoparticles.[38] Slowing down the rate allows

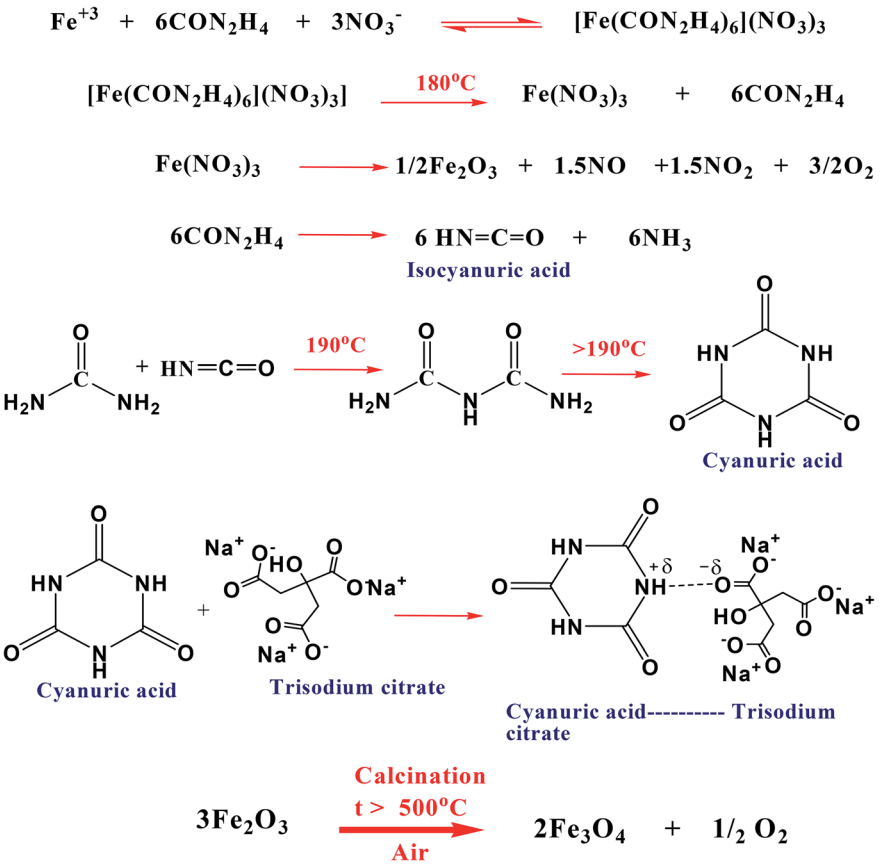

Scheme 2 Possible reactions involved in the formation of Fe_3O_4 by the thermal decomposition method.

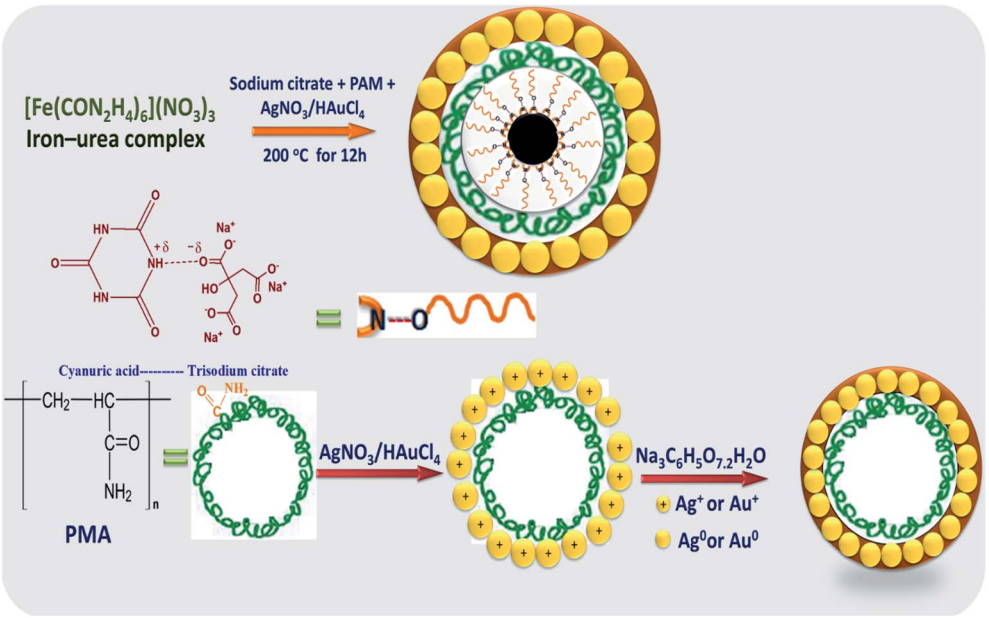

Scheme 3 The suggested mechanism for the formation of Fe_3O_4@M core–shell.

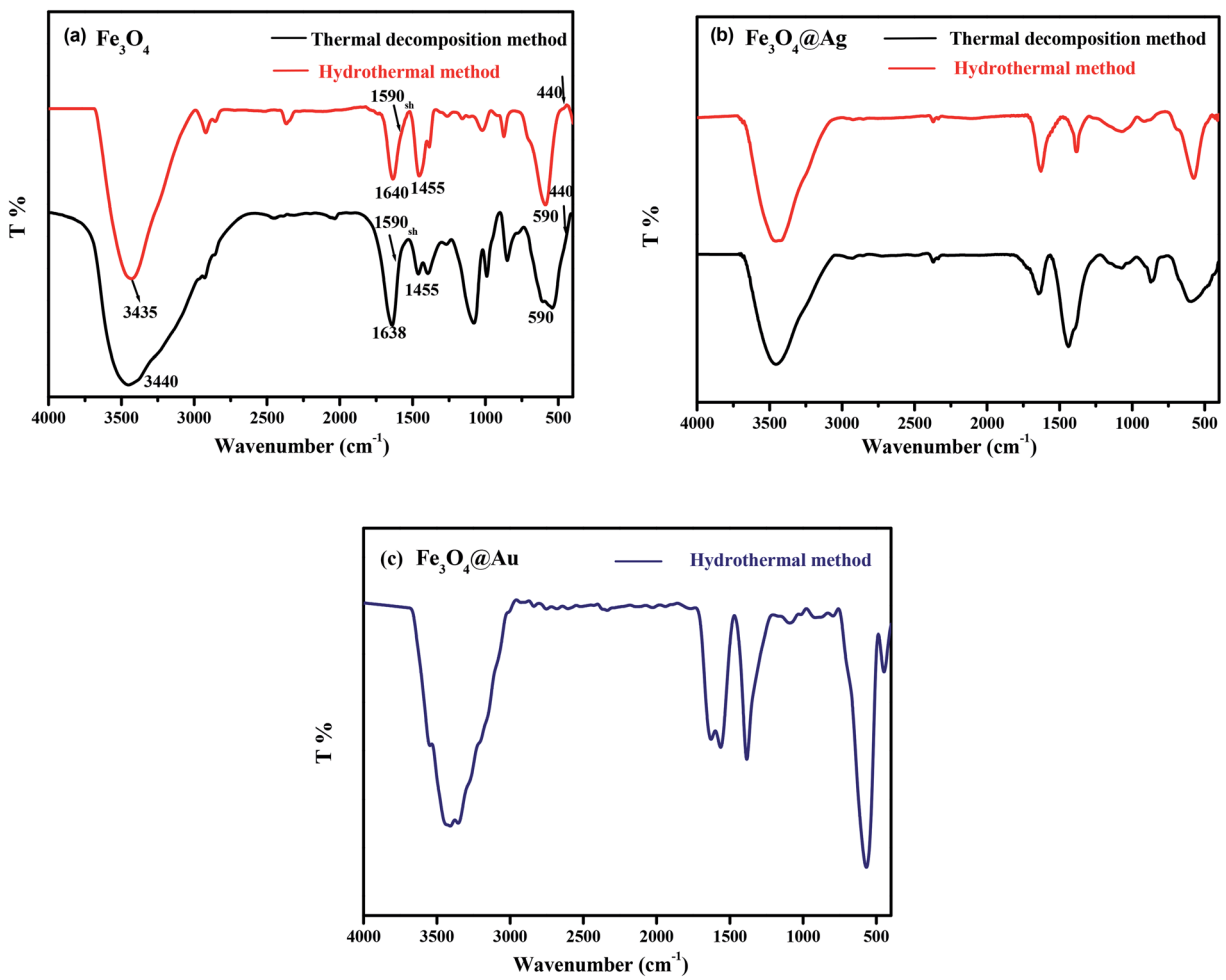

Fig. 1 FT-IR spectra of (a) Fe_3O_4, (b) Fe_3O_4@Ag and (c) Fe_3O_4@Au synthesized by the investigated methods.

primary nanoparticles to have enough time to aggregate into regular spheres.

3.2 Structural characterization of the synthesized nanostructures

Different spectroscopic techniques were utilized to characterize and confirm the structure of the investigated nanostructured materials, Fe_3O_4, Fe_3O_4@Ag and Fe_3O_4@Au synthesized by the two methods.

3.2.1 FT-IR analysis. Analysis of the surface components of the investigated nanostructures was performed with FTIR. FTIR spectra of Fe_3O_4 and core–shell nanospheres formed by the two methods are shown in Fig. 1(a–c). Both FTIR spectra of Fe_3O_4 obtained by the two methods showed a broad peak at 3435 cm^{-1} assigned to the characteristic NH_2 group of PAM and the peak at 1640 cm^{-1} assigned to the characteristic O=C–NH amide group, proving that an amount of $-NH_2$ is embedded on the surface of Fe_3O_4 NPs. The characteristic absorption peaks at 1590 (sh) and 1455 cm^{-1} were assigned to the asymmetric and symmetric vibrations of the carboxylate ion COO^- in trisodium citrate molecules. The two bands appearing around 590 and 440 cm^{-1} correspond to the Fe–O stretching vibrational mode in the tetrahedral site and the Fe–O stretching vibrational mode in an octahedral environment, which confirm the formation of the mixed Fe_3O_4 oxide. Actually, the characteristic IR peaks of Fe_3O_4 synthesized by the two methods shown in Fig. 1(a) are very similar. Fig. 1(b and c) illustrate the FTIR spectra of the Fe_3O_4@Ag core–shell obtained by the two methods and Fe_3O_4@Au by the hydrothermal method. By comparing Fig. 1(b and c) with Fig. 1(a), it was found that there is not much difference between them. The spectra of Fe_3O_4@M (M = Ag or Au) display the well-defined characteristic bands that appeared in the spectrum of Fe_3O_4. The bands were slightly shifted with different relative intensities.

3.2.2 XRD measurements. The phase composition of the prepared nanocatalysts was determined by X-ray powder diffraction. Fig. 2(a–c) show the X-ray diffraction patterns of Fe_3O_4, Fe_3O_4@Ag and Fe_3O_4@Au NPs. The X-ray diffraction pattern of the Fe_3O_4 nanoparticles exhibited peaks at $2\theta = 18.8°$, 30.52°, 35.54°, 43.59°, 53.91°, 57.11°, and 62.89° fully indexed to diffraction from the (111), (220), (311), (400), (422), (511) and (440) planes of the magnetite phases. The sharp and strong

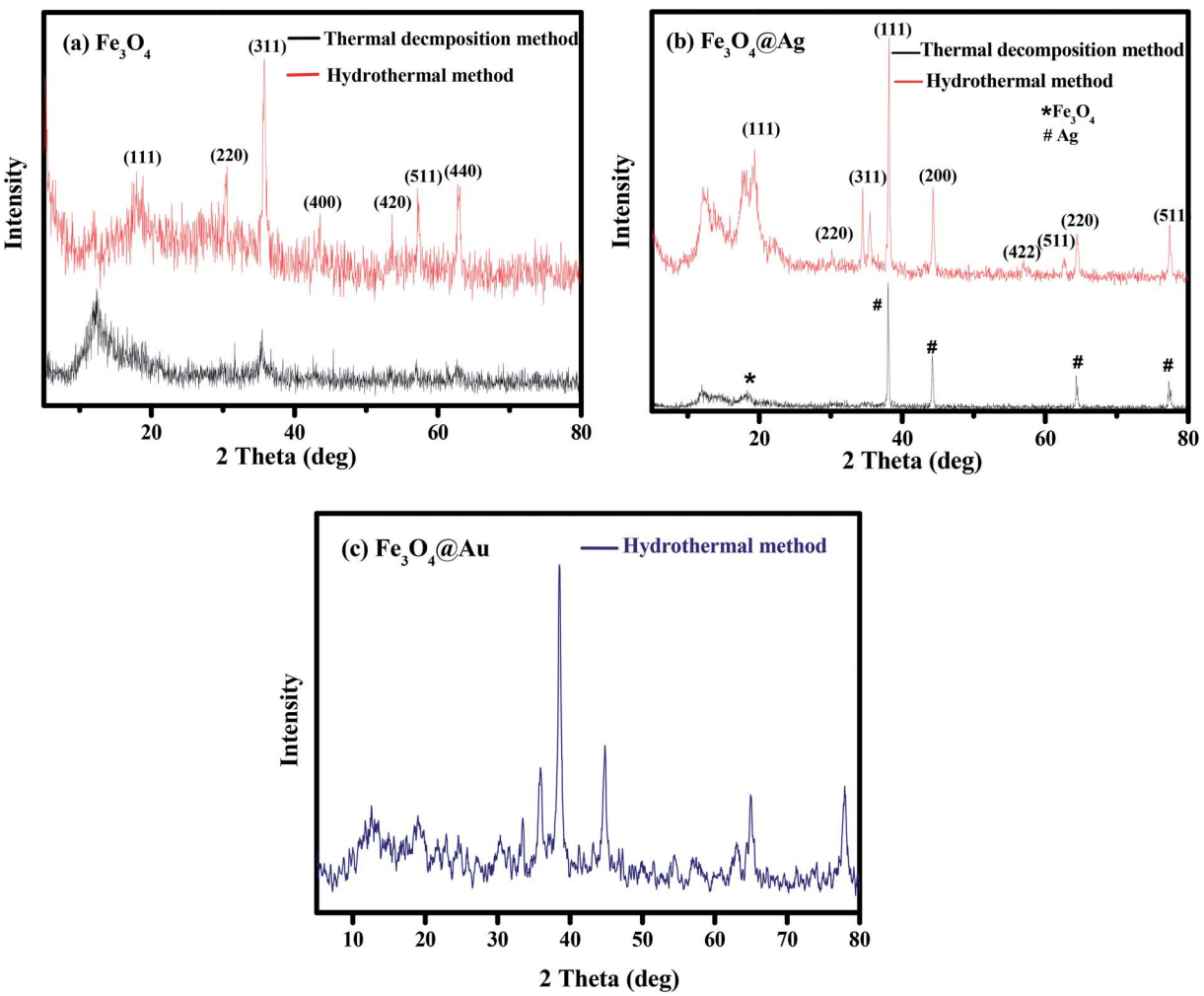

Fig. 2 XRD patterns of (a) Fe_3O_4, (b) Fe_3O_4@Ag and (c) Fe_3O_4@Au synthesized by the investigated methods.

diffraction peaks confirm the crystalline nature of the Fe_3O_4 particles synthesized by the hydrothermal method. But on using the thermal decomposition method, the X-ray diffraction pattern of the Fe_3O_4 NPs showed broad and weak peaks at phases (220), (311), (400) only, indicating the amorphous structure of the synthesized Fe_3O_4. It was observed that the peaks of the synthesized Fe_3O_4 are in agreement with the data of the face centered cubic structure for the reference magnetite in ICDD no. 19:629.[39] The X-ray diffraction pattern of the as-prepared Fe_3O_4@Ag shows the reflection planes (111), (220), (311), (422) and (511) of Fe_3O_4 and an additional four diffraction peaks at $2\theta = 38.1$, 44.3, 64.4 and 77.4 corresponding to the (111), (200), (220) and (511) planes of silver, respectively, indicating the face-centered cubic structure of the nanosilver. But on formation of Fe_3O_4@Ag by the thermal decomposition method, the peak of Fe_3O_4 disappeared completely and only the diffraction peaks of Ag appear. The presence or absence of magnetite peaks in the X-ray diffraction patterns of the Fe_3O_4@Ag core–shell depends on the shell thickness. When the shell has a large thickness, the signal from the core is shielded and becomes invisible in the X-ray diffraction pattern, which was elucidated from measurement of the particle diameter obtained from TEM measurements. The X-ray diffraction pattern of Fe_3O_4@Au core–shell NPs obtained by the hydrothermal method shows two phases of the Fe_3O_4 core and the Au shell. It shows a characteristic diffraction peak at (311) for Fe_3O_4, in addition to four diffraction peaks at 38.1, 44.3, 64.4 and 77.4, corresponding to the (111), (200), (220) and (311) planes of the face-centered cubic structure of Au, respectively.

The crystal size of the synthesized nanoparticles was determined from the width of the X-ray diffraction peaks using the Debye–Scherrer equation for the most intense diffraction peaks for the (220), (311), (400) faces of Fe_3O_4.[40]

$$D = \frac{K\lambda}{\beta \cos \theta}$$

where D is the particle size (nm), λ is the wavelength (0.15406 nm for the X-ray source), β is the full width at half maximum intensity (FWHM) of the peak (radians), and θ is the diffraction angle (radians). Then the average crystalline particle size of Fe_3O_4 was calculated as: $d_{(\text{average})} = D_1 + D_2 + D_3$.

The calculated average crystalline sizes of Fe_3O_4 NPs synthesized by thermal decomposition and hydrothermal methods were found to be 27.75 and 16.02 nm, respectively. While for Fe_3O_4@Ag, they were 69.82 and 29.19 nm for the two previous methods, respectively. The calculated particle size of Fe_3O_4@Au synthesized by the hydrothermal method was found to be 46.93 nm.

Table 1 EDX analysis of synthesized core–shell NPs and mass percentage of each element

	Element mass%				
Core–shell	C	O	Fe	Ag	Au
Fe_3O_4@Ag	9.18	32.84	36.73	21.25	—
Fe_3O_4@Au	8.99	31.10	40.17	—	19.74

3.2.3 Energy dispersive X-ray spectroscopic analysis of synthesized NPs. The energy dispersive X-ray signals provide information about the sample and its composition. EDX spectra measured from the samples imaged by TEM for the synthesized Fe_3O_4@Ag and Fe_3O_4@Au core–shell NPs are shown in Fig. 3(a and b) and their tentative data are collected in Table 1. The EDX analysis has demonstrated that Fe, O, C and Ag are the major elements in Fe_3O_4@Ag, while Fe, O, C and Au are the major elements in Fe_3O_4@Au. These results show that the source of the C element was the trisodium citrate dehydrate coating the Ag or Au NPs. EDX analysis indicated the presence of O and Fe in mass% close to the chemical composition of Fe_3O_4. The mass% of Ag metal is 21.25% which is greater than that of Au which is 19.74%. According to the EDX feedback, it was concluded that each individually synthesized material is consistent with its elements, which further supports the XRD results.

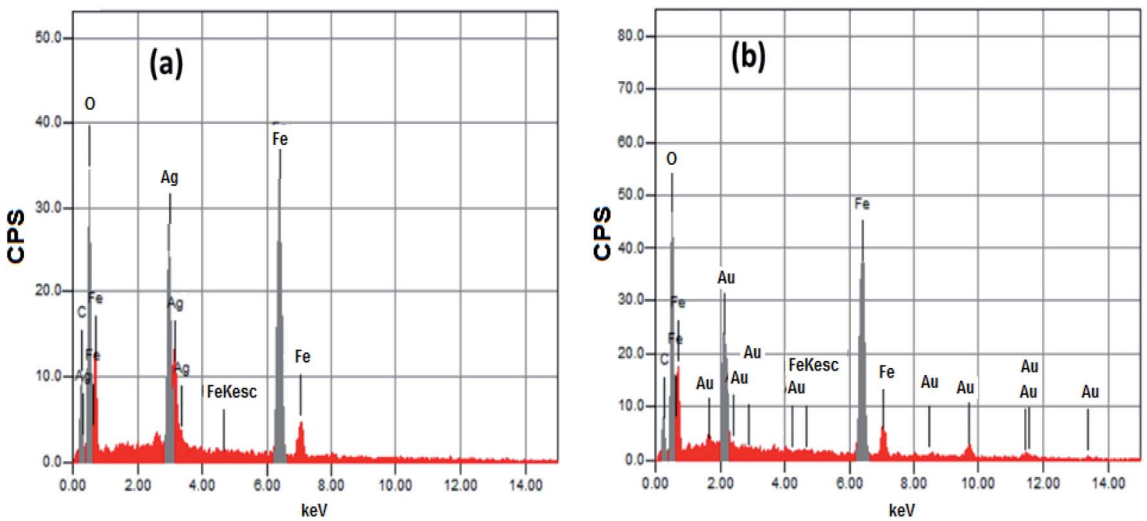

Fig. 3 EDX of (a) Fe_3O_4@Ag and (b) Fe_3O_4@Au core–shell NPs.

3.2.4 TEM analysis of Fe_3O_4@Ag and Fe_3O_4@Au NPs. Transmission electron microscopy (TEM) was used to analyze the morphology, structure and size of the samples prepared by thermal decomposition and hydrothermal methods. Fig. 4(a–f) show the TEM micrographs of Fe_3O_4, Fe_3O_4@Ag and Fe_3O_4@Au nanoparticles. As can observed from the images, the size and morphology of the synthesized NPs are significantly different. Starting with Fe_3O_4, there was a broad random size distribution, near-spherical shapes and slight particle agglomeration (Fig. 4(a)). This is due to the higher magnetostatic coupling between the particles obtained by the thermal decomposition method. In contrast, there was a narrow size distribution, spherical shapes and well-dispersed particles without any agglomeration for the particles formed by the hydrothermal method (Fig. 4(b)). The average size of the Fe_3O_4 nanoparticles synthesized by thermal decomposition is 46.5 nm, while for nanoparticles synthesized by the hydrothermal method it is 21.3 nm, which is nearly half that formed by the other method. Fig. 4(c) shows that Fe_3O_4 nanoparticles were successfully coated with a thick shell of Ag, leading to a spherical core–shell structure for Fe_3O_4@Ag with an average size ≈72.8 nm in the case of the thermal decomposition method, but in the case of the hydrothermal method, there was a thin shell layer of Ag coated magnetite (average size ≈ 27.8 nm) in a prismatic shape, in addition to the spherical shape (Fig. 4(d)). Also, Fe_3O_4@Ag NPs synthesized by the hydrothermal method were more dispersed in nature than those synthesized by thermal decomposition. Based on these observations we decided to use the hydrothermal method for coating Fe_3O_4 with Au. Fe_3O_4@Au NPs exhibited different shapes like rhombic, spherical and square, demonstrating a well-defined core–shell structure of average size ≈ 48.9 nm (Fig. 4(e and f)). The average sizes of all

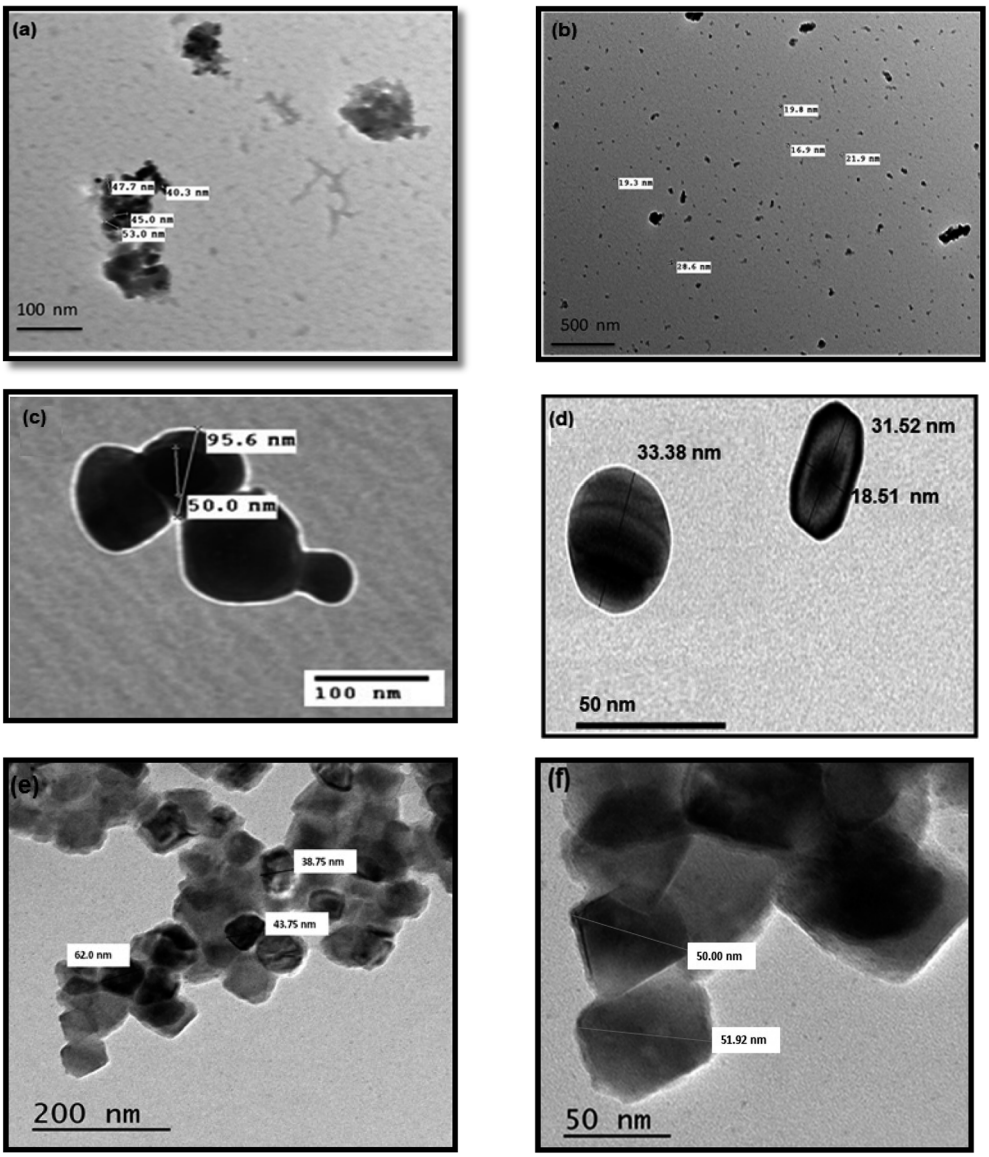

Fig. 4 TEM images of Fe_3O_4 synthesized by (a) thermal decomposition method, (b) hydrothermal method. Fe_3O_4@Ag synthesized by (c) thermal decomposition method, (d) hydrothermal method. (e and f) Fe_3O_4@Au obtained by the hydrothermal method.

synthesized NPs agreed well with the values calculated from XRD using the Debye–Scherrer equation.

3.2.5 Magnetization of Fe_3O_4, Fe_3O_4@Ag and Fe_3O_4@Au NPs. The magnetization properties of Fe_3O_4, Fe_3O_4@Ag and Fe_3O_4@Au NPs synthesized by the two methods were measured by VSM. The relationship between particle size and the magnetic properties of Fe_3O_4 NPs has been reported.[41] The critical size value of Fe_3O_4 NPs indicates the transition from a single-domain to a multi-domain structure. This value depends on the crystal structure whether it is spherical or cubic, or has multiple phases. The critical size for a multi-domain

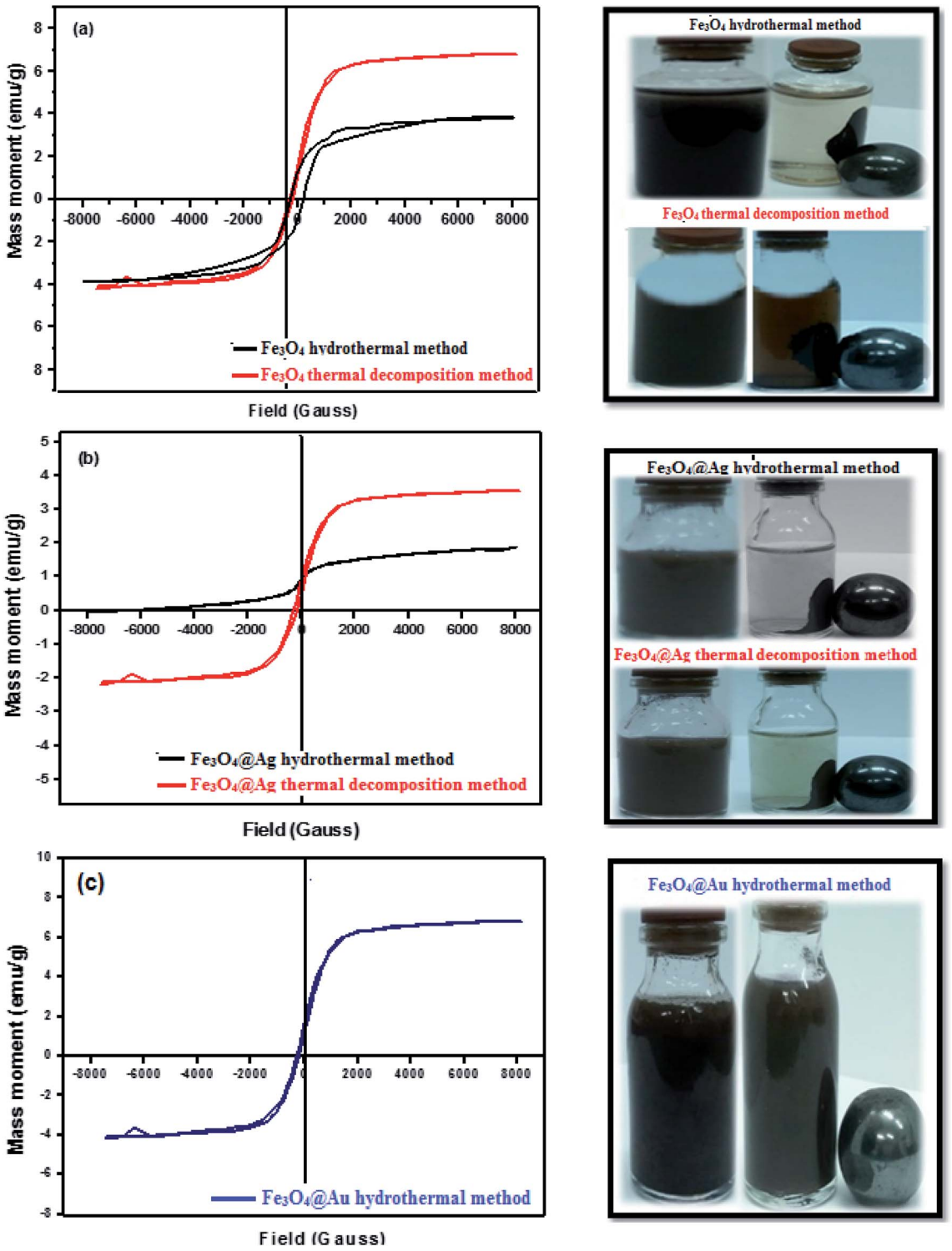

Fig. 5 VSM analysis of (a) Fe_3O_4, (b) Fe_3O_4@Ag obtained by the two investigated methods and (c) Fe_3O_4@Au obtained by the hydrothermal method. Pictures of them dispersed in water: without a magnet, and being attracted by a magnet.

structure has been theoretically estimated to be 128 nm for spherical Fe_3O_4 NPs.[42,43]

Fig. 5(a–c) depict the hysteresis loop of the nanocatalysts measured under a magnetic field varying from −8000 to 8000 Oe at room temperature. Generally, the saturation magnetization, M_g, values of magnetized Fe_3O_4, and Fe_3O_4@Ag nanoparticles decreased from 6.82, and 3.55 emu g^{-1} to 3.9, and 1.99 emu g^{-1} for the nanocatalysts synthesized by the thermal decomposition and hydrothermal methods, respectively. However, the saturation magnetization value of hydrothermal magnetized Fe_3O_4@Au was found to be 6.88 emu g^{-1}. Obviously, the decrease in M_s in the case of Fe_3O_4@Ag relative to Fe_3O_4 is due to the shielding effect of nonmagnetic Ag NPs. However, the saturation magnetization value of Fe_3O_4@Au was greater than that of Fe_3O_4@Ag. This may be due to the liberation of Au NPs from their core–shell, leaving Fe_3O_4 NPs with the same value for its individual case, as will be discussed later in Section 3.3. Also, Fe_3O_4@Ag and Fe_3O_4@Au NPs could be magnetically separated easily from aqueous solution by an external magnet and re-dispersed in water, as shown in the images in Fig. 5(b and c). The outstanding magnetic properties of Fe_3O_4@Ag NPs rendered them economic and reusable for various applications, especially for treatment of wastewater.

3.2.6 TGA analysis of Fe_3O_4, Fe_3O_4@Ag and Fe_3O_4@Au NPs. Fig. 6(a) shows the TGA thermogram of the Fe_3O_4 NPs formed by the two investigated methods, to evaluate the mass percentage of PAM and trisodium citrate on the surface of Fe_3O_4 NPs. The first decomposition stage occurred within the 30–113 °C temperature range for Fe_3O_4 obtained by thermal decomposition and between 30 and 122 °C for that obtained by the hydrothermal method. Steep weight losses of 21.9% and 15.6% were calculated for the NPs obtained from the two methods, respectively, owing to the release of any remaining water and alcohol on the particle surface. The second stage shows weight losses of 12% and 10% over a wide range of temperature, 113–650 °C and 122–685 °C for the nanocatalysts synthesized by the two methods, respectively. This weight loss is due to the PAM decomposition of the thin layer of PAM coating the surface of the Fe_3O_4 NPs in both cases. In the temperature range of 650–800 °C, PAM and the rest of any organic carbon from the citrate were completely decomposed, resulting in weight losses of about 9% and 5%, respectively, for the two

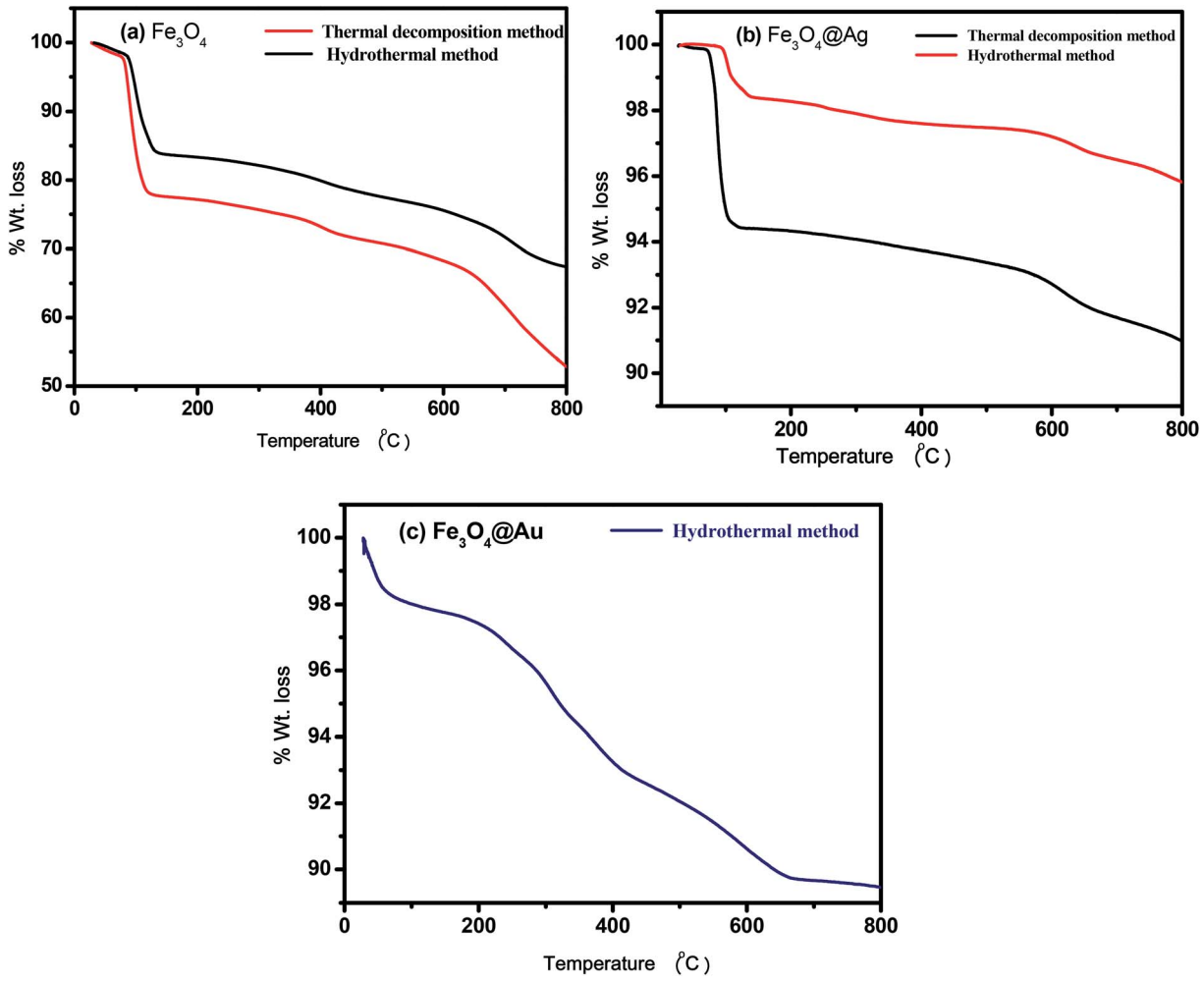

Fig. 6 TGA of (a) Fe_3O_4 formed by hydrothermal and thermal decomposition methods, (b) Fe_3O_4@Ag obtained by hydrothermal and thermal decomposition methods, and (c) Fe_3O_4@Au synthesized by the hydrothermal method.

methods. Then no further weight loss is observed because of the high thermal stability of Fe_3O_4. From these findings, we concluded that Fe_3O_4 NPs synthesized by the hydrothermal method are more thermally stable than those synthesized by thermal decomposition. For Fe_3O_4@Ag and Fe_3O_4@Au core–shell NPs, the thermogravimetric curves (Fig. 6(b and c)) followed the same decomposition profile as Fe_3O_4 NPs but with greater thermal stability, due to the intervention of the noble metals Ag or Au. In fact, the Fe_3O_4@Ag core–shell reflects higher thermal stability than the Fe_3O_4@Au core–shell.

3.3 Kinetics of reductive degradation of the investigated dye

3.3.1 Catalytic degradation of Congo red in water. Herein, the catalytic performance of the Fe_3O_4, Fe_3O_4@Ag and Fe_3O_4@Au core–shell nanocatalysts with $NaBH_4$ as a reducing agent, toward the degradation of CR dye was investigated under ambient conditions. Firstly, the effect of $NaBH_4$ on the degradation of CR was tested, where it was found that $NaBH_4$ alone could not degrade the dye even after 24 h. Similarly, in the absence of $NaBH_4$, the nanocatalyst itself showed no degradation efficiency. This suggested that neither $NaBH_4$ nor the nanocatalyst alone is viable for catalyzing the degradation of CR, and the reaction could be finished quickly only when both the nanocatalyst and $NaBH_4$ were used together. This is due to the fact that the nanocatalyst efficiently catalyzed the reduction of CR by inducing the relay of electrons from BH^{4-} species to the CR dye.

The kinetics of the catalytic reduction of CR using the investigated Fe_3O_4, Fe_3O_4@Ag and Fe_3O_4@Au core–shell nanoparticles was studied using UV-Vis spectroscopy by following the disappearance of the absorbance of CR at $\lambda_{max} = 496$ nm (Fig. 7). The absorption spectra indicated that in the presence of $NaBH_4$, Fe_3O_4, Fe_3O_4@Ag and Fe_3O_4@Au core–shell nanoparticles reduce the intensity of the absorption bands of CR over time intervals, where the band disappeared completely within 35, 16, and 26 min for the mentioned nanocatalysts, respectively. The breakage of the azo group of the CR dye leads to the formation of aromatic amine products (Scheme 4).

An interesting phenomenon occurred when tracking the degradation of the CR using Fe_3O_4@Au, where a bathochromic shift of the absorption band of CR dye by 36 nm was observed on increasing the reaction time, with the formation of an isopiestic point at 593 nm. This was assigned to the liberation of Au NPs in the solution, which has a high plasmonic band and leads to a noticeable overlap in the absorption spectra with increasing time. This observation confirms the higher value of saturation magnetization of Fe_3O_4@Au, as represented in Fig. 5(c).

The efficiencies of removal of CR were found to be 84.2, 96.2, and 91.2% within 35, 16, and 26 min in the presence of Fe_3O_4, Fe_3O_4@Ag and Fe_3O_4@Au NPs, respectively. This clearly shows the higher efficiency of Fe_3O_4@Ag core–shell NPs over those of Fe_3O_4 and Fe_3O_4@Au NPs.

The kinetics of the catalytic reaction were adapted to the pseudo-first-order reaction model, which was used to determine

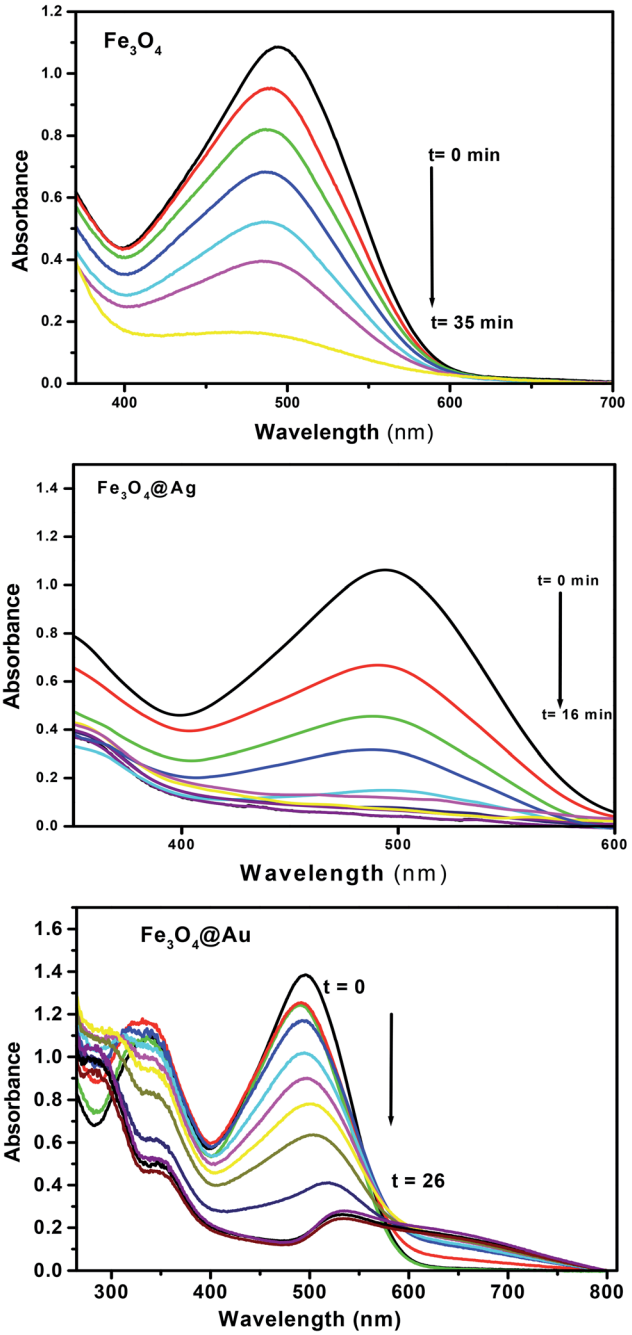

Fig. 7 Absorption spectra of Congo red under the optimum conditions, [CR] = 5×10^{-5} M, [$NaBH_4$] = 2.5×10^{-2} M, and the amount of nanocatalysts = 20 mg, recorded at different time intervals.

the catalytic rate constant, as expressed by the following equation;

$$\ln(A_0/A_t) = kt$$

where A_0 and A_t, are the absorbance of the free CR dye and that at different time intervals; k and t are the catalytic rate constant and the time taken for CR removal in the presence of $NaBH_4$ and the mentioned nanocatalyst. The semi-logarithmic plots are straight lines with a good linear correlation ($r \approx 0.99$)

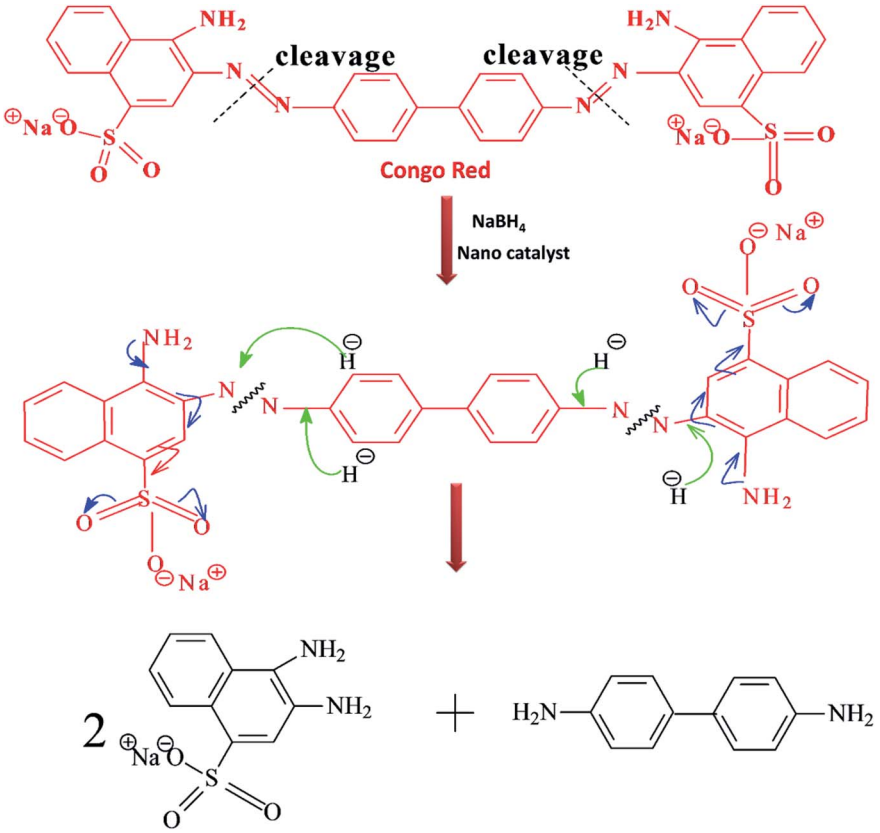

Scheme 4 Proposed mechanism for the reduction of Congo red by $NaBH_4$ catalyzed by the synthesized nanocatalyst.

(Fig. S1†). This confirmed that the degradation reaction follows pseudo-first-order kinetics with respect to the CR dye concentration. The rate constants of degradation of CR dye in the presence of $NaBH_4$ and the nanocatalysts, Fe_3O_4, Fe_3O_4@Ag and Fe_3O_4@Au, were determined from the slopes, and found to be 0.045, 0.16, and 0.09 min^{-1}, respectively. This indicated the highly efficient catalysis of Fe_3O_4@Ag NPs compared to Fe_3O_4@Au and Fe_3O_4 NPs.

Examining the obtained results, it was found that the core–shells, Fe_3O_4@Ag and Fe_3O_4@Au were the most efficient nanocatalysts for the degradation of CR dye over Fe_3O_4 nanoparticles. So the reaction conditions, such as the initial concentration of the dye, the concentration of $NaBH_4$, and the amount of catalyst have been studied considering the two nanocatalysts: Fe_3O_4@Ag and Fe_3O_4@Au core–shells.

3.3.2 Effect of dye concentration. The effect of CR concentration on the degradation rate was investigated at various concentrations (3.0, 4.5, 5.0 and 10.0 $\times$ 10^{-5} M), with the $NaBH_4$ concentration fixed at 2.5 $\times$ 10^{-2} M, and the amount of the nanocatalysts fixed at 20 mg for Fe_3O_4@Ag and

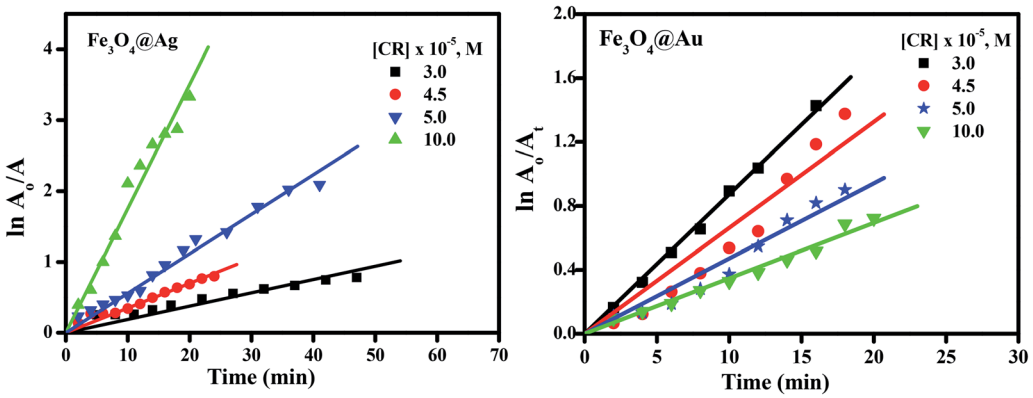

Fig. 8 Pseudo-first-order kinetic plot of ln A_0/A_t *vs.* time for the catalytic degradation of CR dye (3.0–10.0 $\times$ 10^{-5} M), in the presence of $NaBH_4$ (2.5 $\times$ 10^{-2} M), and the nanocatalysts (20 mg for Fe_3O_4@Ag and Fe_3O_4@Au nanoparticles).

Fe_3O_4@Au core–shells. The concentration of $NaBH_4$ was 250–833 times greater than that of CR dye to ensure that the reaction proceeded following pseudo-first-order conditions with respect to the CR dye. The semi-logarithmic plots of the absorbance of CR dye against time are straight lines (Fig. 8), confirming that the catalytic reaction is pseudo-first-order type. The rate constants of the reaction were determined from the slope of the straight lines and were found to be 0.018, 0.035, 0.056, 0.18 min^{-1} for Fe_3O_4@Ag and 0.08, 0.063, 0.048, 0.037 for Fe_3O_4@Au, corresponding to dye concentrations of 3.0, 4.5, 5.0 and 10.0 $\times$ 10^{-5} M, respectively.

It is clear from Fig. 9(a) that the reaction rate increases with an increase in the dye concentration in the presence of Fe_3O_4@Ag as a nanocatalyst, reaching a maximum value of 0.17 min^{-1} at a dye concentration of 1 $\times$ 10^{-4} M. The increase in rate is due to an enhancement of the electron transfer process on the surface of the nanocatalyst, by the generation of electrons as a result of oxidation of Ag^0 to Ag^+ ions, in addition to the electrons of the $NaBH_4$ which leads to an enrichment of the electrons on the surface of the nanocatalysts, and an enhancement in the degradation of CR dye.

However, in the presence of Fe_3O_4@Au as a nanocatalyst, the reaction rate decreases with an increase in the dye concentration, reaching a minimum value of about 0.044 min^{-1} at a dye concentration of 1 $\times$ 10^{-4} M (Fig. 9(b)). The decrease in the rate of catalytic reaction upon increasing the concentration of CR dye may be due to competition between the reaction products or the generated intermediates and the free dye molecules which attach to the catalyst surface. Such interference of reaction products or intermediates will render the catalyst surface poisoned and consequently the dye degradation will ultimately be retarded. A further explanation of this phenomenon is that, when the initial concentration of the dye is increased, more and more dye molecules are adsorbed on the surface of the nanocatalysts. The existence of large amounts of adsorbed dye resulted in the lack of any direct contact with the active sites, thus causing an inhibition effect on the dye degradation.[44]

3.3.3 Effect of $NaBH_4$ concentration. It is known that the concentration of $NaBH_4$, as a reducing agent, influences the catalytic degradation of dye substances. So, the concentration of $NaBH_4$ was varied in the range (1.0–2.5) $\times$ 10^{-2} M, while the concentration of CR dye was kept constant at 5 $\times$ 10^{-5} M, and the amount of nanocatalyst was also kept constant at 20 mg. It was found that the extent of degradation increases upon increasing the $NaBH_4$ concentration, where complete degradation was observed in the presence of 2.5 $\times$ 10^{-5} M $NaBH_4$ at the prescribed reaction time. This observation suggests that an appropriate concentration of BH^{4-} ions is imperative for achieving the best catalytic efficiency of the Fe_3O_4@Ag and Fe_3O_4@Au core–shells. The plots of $\ln(A_t/A_0)$ *vs.* time for CR

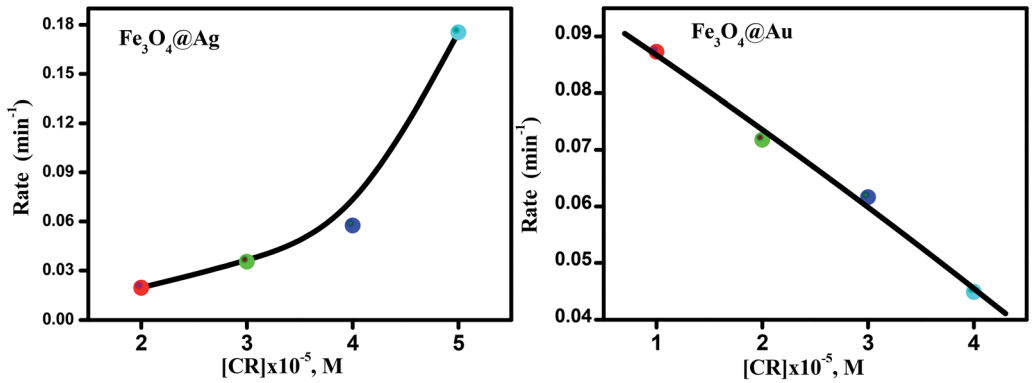

Fig. 9 The effect of dye concentrations on reaction rate, [$NaBH_4$] = 2.5 $\times$ 10^{-2} M, and the amount of catalyst = 20 mg.

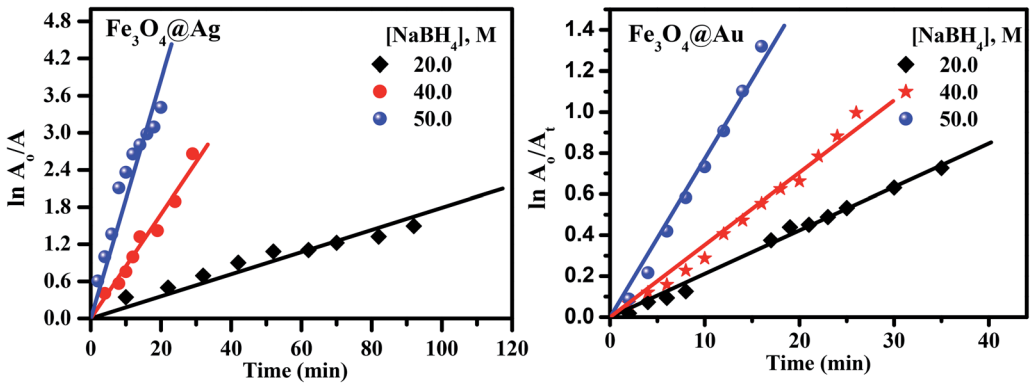

Fig. 10 Pseudo-first-order kinetic plots of ln A_0/A_t *vs.* time for the catalytic degradation of CR dye (5.0 $\times$ 10^{-5} M), with varying concentrations of $NaBH_4$ (1.0–2.5 $\times$ 10^{-2} M), keeping the amount of nanocatalysts constant (20 mg).

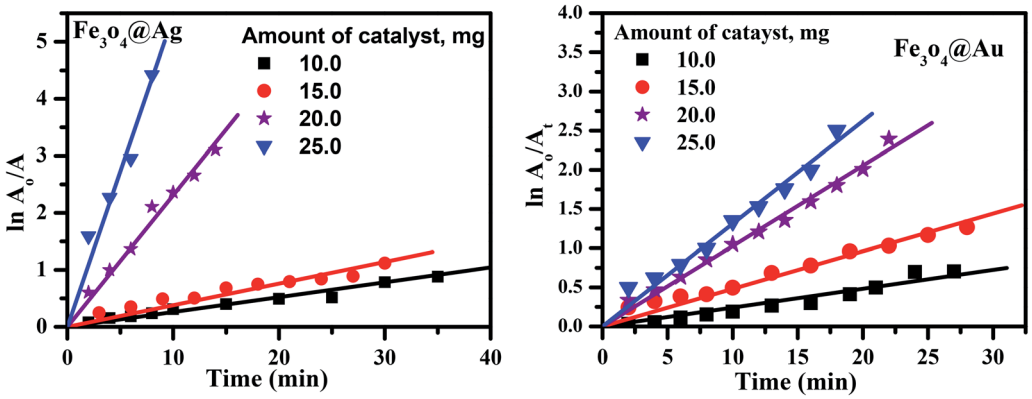

Fig. 11 Pseudo-first-order kinetic plot of ln A_0/A_t *vs.* time (in min) for the catalytic degradation of CR dye (5.0×10^{-5} M), the concentrations of $NaBH_4$ (2.5×10^{-2} M), with a changing amount of nanocatalysts (10–20 mg).

degradation within the range of $NaBH_4$ concentrations are presented in Fig. 10. As can be seen from Fig. S2,† the rate of the reaction increases with an increase in the concentration of $NaBH_4$, due to enhanced electron transfer from BH^{4-} ions to the dye molecules upon raising the concentration of $NaBH_4$.

3.3.4 Effect of the amount of Fe_3O_4@Ag and Fe_3O_4@Au nanocatalysts. In order to investigate the effect of nanocatalyst dose on the degradation of CR, the amount of Fe_3O_4@Ag and Fe_3O_4@Au nanocatalysts was varied from 10 to 20 mg, keeping the other two reaction parameters constant. The degradation profiles of 5.0×10^{-5} M aqueous CR solution over the different amounts of nanocatalyst along with $NaBH_4$ (2.5×10^{-2} M) were investigated. It was found that the degradation efficiency increases as the amount of nanocatalyst increases. This is attributed to the higher availability of surface active sites for the adsorption of BH^{4-} ions and dye molecules. The rate constants were calculated from the slope of the plots of $\ln(A_t/A_0)$ *vs.* time (Fig. 11). The overall results showed an increase in the rate constants with nanocatalyst dose (Fig. S3†). Such an increase was attributed to the increased number of active sites generated with a larger amount of the nanocatalyst. These active sites act as mediators[45] for the electron transfer from the donor to the acceptor molecules, which renders their interaction feasible enough to form the reduction products.

3.3.5 Recycling of Fe_3O_4, Fe_3O_4@Ag, and Fe_3O_4@Au nanocatalysts. The reusability of Fe_3O_4, Fe_3O_4@Ag, and Fe_3O_4@Au nanocatalysts was investigated for the reduction of CR under the optimum reaction conditions which are: [CR] = 5.0×10^{-5} M, and [$NaBH_4$] = 2.5×10^{-2} M at 27 °C. It was found that the Fe_3O_4 nanocatalyst maintained its catalytic activity for one cycle, while the reusability of Fe_3O_4@Ag was evaluated for ten cycles. On the other hand, the catalytic reductive capacity of the Fe_3O_4@Au nanocatalyst was retained for four successive cycles. After every cycle, the nanocatalyst was recovered from the reaction mixture by centrifugation and washed well with ethanol and water. The as-obtained sample was thereafter dried and reused for the next cycle. The relation between the efficiency% and the number of cycles for the catalytic degradation of CR using the prepared nanocatalysts is presented in Fig. 12. It was found that the efficiency% of CR reduction by the regenerated Fe_3O_4@Au nanocatalyst was nearly equal to that of the fresh nanocatalyst even after the repetition of four cycles. However, the Fe_3O_4@Ag nanocatalyst showed a slight loss in its capacity after the fifth cycle, as indicated by the small decrease in the catalytic efficiency. After the sixth cycle, a dramatic decrease in the catalytic efficiency was observed. The decrease in the efficiency is due to the loss of catalyst during separation, so the number of reactive surface sites for adsorption of CR and BH^{4-} decreases.

A quick review of the literature relevant to the degradation of CR by different methods is summarized in Table 2. This reveals that degradation of CR dye is carried out using Fe_3O_4 based nanocomposites in different systems, such as catalytic reduction, photo-degradation and adsorption using Fe_3O_4@Ag hydrothermally synthesized in the present study. As shown from this review, an excellent catalytic degradation for CR dye with fantastic recyclability reaching 10 cycles without any considerable loss of the catalyst efficiency was achieved using our catalyst.

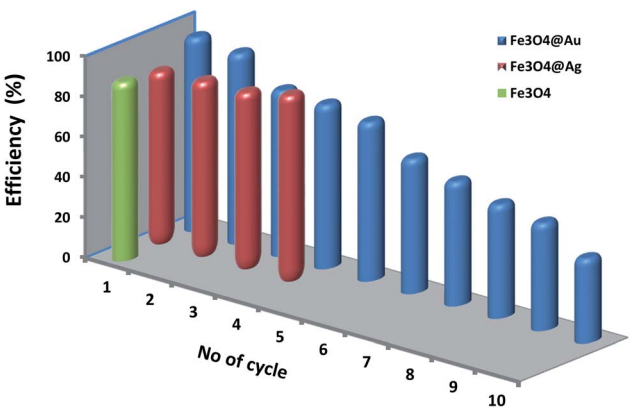

Fig. 12 The relation between catalytic efficiency of Fe_3O_4, Fe_3O_4@Ag, and Fe_3O_4@Au nanocatalysts and the number of cycles of CR dye reduction.

Table 2 Catalytic parameters of Fe_3O_4-based nanocatalysts for the degradation of Congo red

Catalyst	Method	Reaction time (min)	Efficiency%	Weight	No. of cycles	Reference
Fe_3O_4@PANI@Au	Reduction $NaBH_4$	20	100	10 mg	5	46
Fe_3O_4/MgAl-LDH	Adsorption	30	100	80 mg	—	47
Fe_3O_4–PbS	UV-photo degradation	120	80	—	—	48
Fe_3O_4@BTCA	Adsorption	20	97	20 mg	5	49
1,2,4,5-Benzenetetracarboxylic acid BTCA						
Fe_3O_4–Ag nanoalloys	Adsorption	4	92	30 μg	—	46
Fe_3O_4@Ag (present work)	Reduction $NaBH_4$	16	96	20 mg	10	—

4. Conclusion

Herein, highly efficient and reusable nanocatalysts, Fe_3O_4@Ag and Fe_3O_4@Au, have been synthesized by utilizing a facile and economic synthesis using a hydrothermal method which showed excellent CR dye reduction ability in the presence of $NaBH_4$ as a reducing agent *via* an electron-relaying process. The reduction followed pseudo-first-order kinetics and the rate of the reaction depends greatly on the concentration of the dye, $NaBH_4$ and the nanocatalyst. The excellent catalytic activity and good reusability suggest that the Fe_3O_4@Ag, and Fe_3O_4@Au nanocatalysts could be used as potential candidates for the treatment of industrially discharged wastewater.

Conflicts of interest

There are no conflicts to declare.

Acknowledgements

The authors are grateful to the Scientific Research Fund at Tanta University, Egypt for funding this work through research project code TU:02-19-03.

References

1 B. J. Kim, T. Park, H. C. Moon, S.-Y. Park, D. Hong, E. H. Ko, J. Y. Kim, J. W. Hong, P. S. Woo, Y.-G. Kim and I. S. Choi, Cytoprotective Alginate/Polydopamine Core/Shell Microcapsules in Microbial Encapsulation, *Angew. Chem., Int. Ed.*, 2014, **53**, 14443–14446, DOI: 10.1002/anie.201408454.

2 T. Ozel, G. R. Bourret, A. L. Schmucker, K. A. Brown and C. A. Mirkin, Hybrid semiconductor core-shell nanowires with tunable plasmonic nanoantennas, *Adv. Mater.*, 2013, **25**, 4515–4520, DOI: 10.1002/adma.201301367.

3 Z. Shan, D. Clayton, S. Pan, P. S. Archana and A. Gupta, Visible Light Driven Photoelectrochemical Properties of Ti@TiO_2 Nanowire Electrodes Sensitized with Core–Shell Ag@Ag_2S Nanoparticles, *J. Phys. Chem. B*, 2014, **118**, 14037–14046, DOI: 10.1021/jp504346k.

4 C. R. Ghosh and S. Paria, Core/shell nanoparticles: classes, properties, synthesis mechanisms, characterization, and applications, *Chem. Rev.*, 2012, **112**, 2373–2433, DOI: 10.1021/cr100449n.

5 L. Yang, W. Luo and G. Cheng, Graphene-Supported Ag-Based Core–Shell Nanoparticles for Hydrogen Generation in Hydrolysis of Ammonia Borane and Methylamine Borane, *ACS Appl. Mater. Interfaces*, 2013, **5**, 8231–8240, DOI: 10.1021/am402373p.

6 M. B. Gawande, A. Goswami, T. Asefa, H. Guo, A. V. Biradar, D.-L. Peng, R. Zboril and R. S. Varma, Core-shell nanoparticles: synthesis and applications in catalysis and electrocatalysis, *Chem. Soc. Rev.*, 2015, **44**, 7540–7590, DOI: 10.1039/c5cs00343a.

7 R. Liu and R. D. Priestley, Rational design and fabrication of core–shell nanoparticles through a one-step/pot strategy, *J. Mater. Chem. A*, 2016, **4**, 6680–6692, DOI: org/10.1039/C5TA09607C.

8 A. K. Gupta and M. Guptab, Synthesis and surface engineering of iron oxide nanoparticles for biomedical applications, *Biomaterials*, 2005, **26**, 3995–4021, DOI: org/10.1016/j.biomaterials.2004.10.012.

9 W. Fang, J. Zheng, C. Chen, H. Zhang, Y. Lu, L. Mac and G. Chen, One-pot synthesis of porous Fe3O4 shell/silver core nanocomposites used as recyclable magnetic antibacterial agents, *J. Magn. Magn. Mater.*, 2014, **357**, 1–6, DOI: 10.1016/j.jmmm.2014.01.024.

10 S. E. Lyshevski, *Dekker encyclopedia of nanoscience and nanotechnology*, CRC Press, Boca Raton, 3rd edn, 2014, p. 7.

11 L. R. Harivardhan, J. L. Arias, J. Nicolas and P. Couvreur, Magnetic Nanoparticles: Design andCharacterization, Toxicity and Biocompatibility, Pharmaceutical and Biomedical Applications., *Chem. Rev.*, 2012, **112**, 5818–5878, DOI: 10.1021/cr300068p.

12 K. Ulbrich, K. Hol, V. Subr, A. Bakandritsos, J. Tucek and R. Zboril, Magnetic Nanoparticles: Design and Characterization, Toxicity and Biocompatibility, Pharmaceutical and Biomedical Applications, *Chem. Rev.*, 2016, **116**, 5338–5431, DOI: 10.1021/acs.chemrev.5b00589.

13 S. Laurent, L. Vander Elst and R. N. Muller, Superparamagnetic iron oxide nanoparticles for MRI, *The chemistry of contrast agents in medical magnetic resonance imaging*, 2013, vol. 10, pp. 427–447.

14 S. Laurent, D. Forge, M. Port, A. Roch, C. Robic, L. E. Vander and R. N. Muller, Magnetic Iron Oxide Nanoparticles:

Synthesis, Stabilization, Vectorization, Physicochemical Characterizations, and Biological Applications, *Chem. Rev.*, 2008, **108**, 2064–2110, DOI: 10.1021/cr068445e.

15 H. Shokrollahi, Structure, synthetic methods, magnetic properties and biomedical applications of ferrofluids, *Mater. Sci. Eng., C*, 2013, **33**, 2476–2487, DOI: 10.1016/j.msec.2013.03.028.

16 J.-M. Li, A. C. H. Huan, L. Wang, Y.-W. Du and D. Feng, Interface effects on magnetoresistance and magnetic-field-reduced Raman scattering in magnetite, *Phys. Rev. B: Condens. Matter Mater. Phys.*, 2000, **61**, 6876, DOI: 10.1103/PhysRevB.61.6876.

17 R. R. Castillo and M. Vallet-Regí, Functional Mesoporous Silica Nanocomposites: Biomedical Applications and Biosafety, *Int. J. Mol. Sci.*, 2019, **20**, 929, DOI: 10.3390/ijms20040929.

18 J.-M. Li, X.-L. Zeng and Z.-A. Xu, Partial cationic inversion-induced magnetic hardening of densely packed 23-nm-sized nanocrystallite-interacting nickel ferrite electrospun nanowires, *Appl. Phys. Lett.*, 2013, **103**, 232410, DOI: 10.1063/1.4840320.

19 C. F. Bohren and D. R. Huffman, *Absorption and scattering of light by small particles*, Wiley-VCH, 2008.

20 M. Rai, A. P. Ingle, S. Birla, A. Yadav and C. A. Dos Santos, Strategic role of selected noble metal nanoparticles in medicine, *Crit. Rev. Microbiol.*, 2016, **42**, 696–719, DOI: 10.3109/1040841x.2015.1018131.

21 P. Gong, H. Li, X. He, K. Wang, J. Hu, W. Tan, S. Zhang and X. Yang, Nanotechnology Preparation and antibacterial activity of Fe_3O_4@Ag nanoparticles, *Nanotechnology*, 2007, **18**, 285604, DOI: 10.1088/0957-4484/18/28/285604.

22 B. Chudasama, A. K. Vala, N. Andhariya, R. V. Upadhyay and R. V. Mehta, Enhanced antibacterial activity of bifunctional Fe_3O_4-Ag core-shell nanostructures, *Nano Res.*, 2009, **2**, 955–965, DOI: 10.1007/s12274-009-9098-4.

23 A. Amarjargal, L. D. Tijing, I. T. Im and C. S. Kim, Simultaneous preparation of Ag/Fe3O4 core–shell nanocomposites with enhanced magnetic moment and strong antibacterial and catalytic properties, *Chem. Eng. J.*, 2013, **226**, 243–254, DOI: 10.1016/j.cej.2013.04.054.

24 W. Q. Jiang, Y. F. Zhou, Y. L. Zhang, S. H. Xuan and X. L. Gong, Superparamagnetic Ag@Fe_3O_4core-shell nanospheres: fabrication, characterization and application as reusable nanocatalysts, *Dalton Trans.*, 2012, **41**, 4594–4601, DOI: 10.1039/c2dt12307j.

25 J. Park, K. An, Y. Hwang, J.-G. Park, H.-J. Noh, J.-Y. Kim, J.-H. Park, N.-M. Hwang and T. Hyeon, Ultra-large-scale syntheses of monodisperse nanocrystals, *Nat. Mater.*, 2004, **3**, 891–895, DOI: 10.1038/nmat1251.

26 J. S. Salazar, L. Perez, O. D. Abril, L. P. Truong, D. Ihiawakrim, M. Vazquez, G. Jean-Marc, S. Begin-Colin and G. Pourroy, Magnetic Iron Oxide Nanoparticles in 10−40 nm Range: Composition in Terms of Magnetite/Maghemite Ratio and Effect on the Magnetic Properties, *Chem. Mater.*, 2011, **23**, 1379–1386, DOI: 10.1021/cm103188a.

27 S. Ge, X. Shi, K. Sun, C. Li, C. Uher, J. R. Baker, M. M. BanaszakHoll and B. G. Orr, Facile hydrothermal synthesis of iron oxide nanoparticles with tunable magnetic properties, *J. Phys. Chem. C*, 2009, **113**, 13593–13599, DOI: 10.1021/jp902953t.

28 H. Cai, X. An, C. Jun, J. Li, S. Wen, K. Li, M. Shen, L. Zheng, G. Zhang and X. Shi, Facile hydrothermal synthesis and surface functionalization of polyethyleneimine-coated iron oxide nanoparticles for biomedical applications., *ACS Appl. Mater. Interfaces*, 2013, **5**, 1722–1731, DOI: 10.1021/am302883m.

29 Y. B. Khollam, S. R. Dhage, H. S. Potdar, S. B. Deshpande, P. P. Bakare, S. D. Kulkarni and S. K. Date, Microwave hydrothermal preparation of submicron-sized spherical magnetite (Fe_3O_4) powders, *Mater. Lett.*, 2002, **56**, 571–577, DOI: 10.1016/S0167-577X(02)00554-2.

30 J. Li, X. Shi and M. Shen, Hydrothermal Synthesis and Functionalization of Iron Oxide Nanoparticles for MR Imaging Applications, *Part. Part. Syst. Charact.*, 2014, **31**, 1223–1237, DOI: 10.1002/ppsc.201400087.

31 S. A. M. Khawja Ansari, F. Eleonora, R. F. Alessandro, S. Ilaria, A. Monica, A. Ornella, C. Roberta, G. Caterina and D. Federico, Magnetic Iron Oxide Nanoparticles: Synthesis, Characterization and Functionalization for Biomedical Applications in the Central Nervous System, *Materials*, 2019, **12**, 465, DOI: 10.3390/ma12030465.

32 Á. D. Jesús Ruz-Baltazar, Green synthesis assisted by sonochemical activation of Fe_3O-Ag nano-alloys: Structural characterization and studies of sorption of cationic dyes, *Inorg. Chem. Commun.*, 2020, **120**, 108148, DOI: 10.1016/j.inoche.2020.108148.

33 N. Mizutani, T. Iwasaki and S. Watano, Response Surface Methodology Study on Magnetite Nanoparticle Formation under Hydrothermal Conditions, *Nanomater. Nanotechnol.*, 2015, **5**, 1–7, DOI: 10.5772/60649.

34 W. Wu, Z. Wu, T. Yu, C. Jiang and W. S. Kim, Recent progress on magnetic iron oxide nanoparticles: synthesis, surface functional strategies and biomedical applications, *Sci. Technol. Adv. Mater.*, 2015, **16**, 023501, DOI: 10.1088/1468-6996/16/2/023501.

35 G. Sharma and P. Jeevanandam, Synthesis of self-assembled prismatic iron oxide nanoparticles by a novel thermal decomposition route, *RSC Adv.*, 2013, **3**, 189, DOI: 10.1039/C2RA22004K.

36 Y. Zhu, Y. Qian, X. Li and M. Zhang, A nonaqueous solution route to synthesis of polyacrylamide-silver nanocomposites at room temperature, *Nanostruct. Mater.*, 1998, **10**, 673–678, DOI: 10.1016/S0965-9773(98)00096-8.

37 Y. Peng, A. W. Xu, B. Deng, M. Antonietti and H. Colfen, Polymer-controlled crystallization of zinc oxide hexagonal nanorings and disks, *J. Phys. Chem. B*, 2006, **110**, 2988–2993, DOI: 10.1021/jp056246d.

38 G. Z. Wang, R. Saeterli, P. M. Rorvik, A. T. J. van Helvoort, R. Holmestad, T. Grande and M. A. Einarsrud, Self-Assembled Growth of $PbTiO_3$ Nanoparticles into Microspheres and Bur-like Structures, *Chem. Mater.*, 2007, **19**, 2213, DOI: 10.1021/cm063047d.

39 M. Yamaura and D. A. Fungaro, Synthesis and characterization of magnetic adsorbent preparedby magnetite nanoparticles and zeolite from coal fly ash, *J. Mater. Sci.*, 2013, **48**, 5093–5101, DOI: 10.1007/s10853-013-7297-6.

40 S.-J. Cho, J.-C. Idrobo, J. Olamit, K. Liu, N. D. Browning and S. M. Kauzlarich, Growth Mechanisms and Oxidation-Resistance of Gold-Coated Iron Nanoparticles, *Chem. Mater.*, 2005, **17**, 3181–3186, DOI: 10.1021/cm0500713.

41 Q. Li, C. W. Kartikowati, S. Horie, T. Ogi, T. Iwaki and K. Okuyama, Correlation between particle size/domain structure and magnetic properties of highly crystalline Fe_3O_4 nanoparticles, *Sci. Rep.*, 2017, **7**, 9894, DOI: 10.1038/s41598-017-09897-5.

42 R. F. Butler and S. K. Banerjee, Theoretical single-domain grain-size range in magnetite and titanomagnetite, *J. Geophys. Res.*, 1975, **80**, 4049–4058, DOI: 10.1029/JB080i029p04049.

43 D. L. Leslie-Pelecky and R. D. Rieke, Magnetic Properties of Nanostructured Materials, *Chem. Mater.*, 1996, **8**, 1770–1783, DOI: 10.1021/cm960077f.

44 N. Shimizu, C. Ogino, M. F. Dadjour and T. Murata, Sonocatalytic degradation of methylene blue with TiO_2 pellets in water, *Ultrason. Sonochem.*, 2007, **14**, 184–190, DOI: 10.1016/j.ultsonch.2006.04.002.

45 S. Gupta, C. Giordano, M. Gradzielski and S. K. Mehta, Microwave-assisted synthesis of small Ru nanoparticles and their role in degradation of congo red, *J. Colloid Interface Sci.*, 2013, **411**, 173–181, DOI: 10.1016/j.jcis.2013.08.030.

46 M. Chen, P. Liu, C. Wang, W. Ren and G. W. Diao, Fast catalytic reduction of an azo dye by recoverable and reusable Fe_3O_4@PANI@Au magnetic composites, *New J. Chem.*, 2014, **38**, 4566–4573, DOI: 10.1039/C4NJ00806E.

47 R. Shan, L. Yan, K. Yang, S. Yu, Y. Hao, H. Yu and B. Du, Magnetic Fe_3O_4/MgAl-LDH composite for effective removal of three red dyes from aqueous solution, *Chem. Eng. J.*, 2014, **15**, 38–46, DOI: 10.1016/j.cej.2014.04.105.

48 K. Hedayati, M. Goodarzi and M. Kord, Green and facile synthesis of Fe_3O_4-PbS magnetic nanocomposites applicable for the degradation of toxic organic dyes, *Main Group Met. Chem.*, 2016, **39**, 183–194, DOI: 10.1515/mgmc-2016-0027.

49 S. Chatterjee, N. Guha, S. Krishnan, A. K. Singh, P. Mathur and D. K. Rai, Selective and Recyclable Congo Red Dye Adsorption by Spherical Fe_3O_4 Nanoparticles Functionalized with 1,2,4,5-Benzenetetracarboxylic Acid, *Sci. Rep.*, 2020, **10**, 111, DOI: 10.1038/s41598-019-57017-2.